LOW-RANK RADIOSITY USING SPARSE MATRICES

Eduardo Fernández[1], Pablo Ezzatti[1], Sergio Nesmachnow[1] and Gonzalo Besuievsky[2]
[1]*Centro de Cálculo, Universidad de la República, Montevideo, Uruguay*
[2]*Geometry and Graphics Group, Universitat de Girona, Girona, Spain*

Keywords: Radiosity, Real-time Global Illumination.

Abstract: Radiosity methods are part of the global illumination techniques, which deal with the problem of generating photorealistic images in 3D scenes with Lambertian surfaces. Low-rank radiosity is a $O(nk)$ method, where n is the number of polygons and k is the rank of the matrix used as a direct transport operator. This method allows calculating, in real-time and with infinite bounces, the illumination of a scene with static geometry and dynamic lighting. In this paper we present a new methodology for low-rank radiosity calculation based on the use of sparse matrices, which significantly reduces the memory storage required and achieves speedup improvements over the original low-rank method. Experimental analysis was performed in both traditional computers and new graphics processing unit architectures.

1 INTRODUCTION

The radiosity method is a pioneering technique for global illumination on scenes with Lambertian surfaces, which has been applied in many areas of design and computer animation (Dutre et al., 2006).

Since the classic formulation of the radiosity technique in the decade of 1980, several iterative resolution methods have been proposed (Cohen et al., 1993). These methods are not feasible for computing realistic images in real-time (many bounces at 20 fps), due to their iterative nature. After that, several other methods have been proposed to achieve the real-time computation of the global illumination, such as *instant radiosity* (Keller, 1997), *precomputed radiance transfer* (Sloan et al., 2002), *radiance transport* (Kontkanen et al., 2006; Lehtinen et al., 2008) and *photon mapping* (Wang et al., 2009), which have shown some success using global illumination approximations.

By exploiting spatial coherence, the low-rank radiosity method (LRR) (Fernández, 2009) allows solving the real-time radiosity problem with infinite bounces, for scenes with static geometry and dynamic lighting, using a low memory storage approach. The original LRR implementation used full matrices, and the promising idea of generating sparse matrices was previously pointed out, but it was not developed.

This work presents a new approach for the utilization of sparse matrices in the LRR method. Specific implementations of algorithms to solve the radiosity problem in both traditional computer architectures (CPU) and modern graphic processing units (GPU) are introduced. The experimental results show that the GPU implementation of the LRR method based on sparse matrices has an acceleration factor greater than four, compared with the full matrix approach of the LRR method. These promising results demonstrate that our approach is an alternative for real-time radiosity applications. Comparing to other strategies, LRR ensures always a full global illumination solution being capable of dealing efficiently with environments with significant indirect illumination contribution.

The rest of the article is organized as follows. Section 2 introduces the radiosity problem and the previous work. The low-rank radiosity method is described in Section 3. Section 4 introduces the utilization of sparse matrices in LRR, and describes the implementations of the proposed algorithms for sparse low-rank radiosity in CPU and GPU. The experimental analysis is reported in Section 5. Finally, Section 6 summarizes the conclusions of the research and formulates the main lines for future work.

2 THE RADIOSITY PROBLEM

This section starts by introducing the radiosity problem formulation. After that, the main proposals found in the literature related with the pre-computed radiosity and radiance transfer problem are reviewed.

Fernández E., Ezzatti P., Nesmachnow S. and Besuievsky G..
LOW-RANK RADIOSITY USING SPARSE MATRICES.
DOI: 10.5220/0003829402600267
In *Proceedings of the International Conference on Computer Graphics Theory and Applications* (GRAPP-2012), pages 260-267
ISBN: 978-989-8565-02-0

2.1 Problem Formulation

The radiosity problem is modeled by a Fredholm integral equation, the *radiosity equation* (1). In Equation 1, $B(x)$ is the radiosity in the point x, $E(x)$ is the light emission in x, $\rho(x)$ is the Lambertian diffuse reflectivity of x, and $G(x,x')$ is a geometric factor that determines how much the radiosity in x' contributes to the radiosity of x (Cohen et al., 1993).

$$B(x) = E(x) + \rho(x) \int_S B(x')G(x,x')dA' \qquad (1)$$

Any Fredholm equation can be transformed into a discrete equation, which implies solving a linear system. In the radiosity problem the linear system is expressed by Equation 2, where $\mathbf{I}$ is the identity matrix with dimension $n \times n$ (n is the number of polygons), $\mathbf{R}$ is a diagonal matrix that stores the reflectivity of the polygons, $\mathbf{F}$ is the matrix with the form factors $\mathbf{F}_{ij}$ –which indicate the fraction of light reflected by the polygon i that arrives to the polygon j–, B is a vector with the radiosity value of each patch, and E is the vector with the emission of each patch.

$$(\mathbf{I} - \mathbf{RF})B = E \qquad (2)$$

This discrete equation can be also formulated through the use of a direct transport operator $\mathbf{T}$, which expresses the direct transmission of light between two surfaces of the scene. Using $\mathbf{T}$, the discrete radiosity equation (Equation 2) is expressed as $(\mathbf{I} - \mathbf{T})B = E$. Moreover, the operator $\mathbf{G} = (\mathbf{I} - \mathbf{T})^{-1}$, is a global transport operator relating the emitted light with the final radiosity of the scene, $B = \mathbf{G}E$. For scenes where the geometry is fixed and only the light output varies, the operators $\mathbf{T}$ and $\mathbf{G}$ are constant.

2.2 Related Work

The main class of elements used in light transport includes the polygons, the parametric surfaces (Cohen et al., 1993), and the discrete points (Fasshauer, 2006). In all these cases it is possible to build operators $\mathbf{T}$ and $\mathbf{G}$ that indicate the transport relationship between any pair of elements.

The $O(n^2)$ memory required to store $\mathbf{T}$ has been clearly posed as a problem in early radiosity papers (Cohen et al., 1988). Many solutions have been proposed, such as two-level hierarchy (Cohen et al., 1986), hierarchical structures (Hanrahan et al., 1991), and wavelets (Gortler et al., 1993). The memory savings are determined by the spatial coherence of the scenes, where it is highly probable that neighboring elements i, j have similar transport values with many other elements k of the scene, that is, $\mathbf{T}_{ik} \approx \mathbf{T}_{jk}$. In this case, these values are considered equal, then, many transport values can be replaced by a single value. This is the main idea behind the hierarchical approximation $H(\mathbf{T})$ of any $\mathbf{T}$ operator, where $H(\mathbf{T})$ is usually stored in $O(n)$ memory. The balance between the error introduced by the method and the memory saved is highly convenient for most scenes. In these works the calculation of B is done by iterative methods, avoiding the need of computing $H(\mathbf{G})$.

Recently, other kinds of methods that include BRDF surfaces and the calculation of $H(\mathbf{G})$ have been developed. In (Kontkanen et al., 2006), the BRDF operator ($\mathbf{T}$) is transformed into $H(\mathbf{T})$ through the use of wavelets, and $H(\mathbf{G})$ is calculated using the Neumann series $H(\mathbf{G}) = \mathbf{I} + H(\mathbf{T}) + H(\mathbf{T})^2 + \ldots$, by removing all values of $H(\mathbf{T})^n$ smaller than a certain threshold. After calculating the global incident radiance of a scene, the BRDF function is applied again to find an image from a particular point of view. Later, in (Lehtinen et al., 2008) a meshless hierarchical representation of the objects in the scene, built upon a hierarchy of points, is performed. Each point consists of a pair (position, normal) and has a radius of influence related with the hierarchy level to which it belongs. Using a hierarchical function basis, a sparse matrix $H(\mathbf{T})$ is generated by elimination of all terms below a threshold, and a final sparse operator $H(\mathbf{G} - \mathbf{I})$ is created, using also Neumann series.

Other methods to achieve real-time global illumination are based on instant radiosity techniques (Keller, 1997) and its variants (Laine et al., 2007), but these methods compute only a few bounces.

In contrast, the LRR method proposed in this work allows to solve the radiosity problem with infinite bounces and relatively small computational resources. This result is based on the premise that when $\mathbf{T}$ is a low-rank matrix, the operator $\mathbf{G}$ can be easily calculated, as it is explained in the next section.

3 THE LOW-RANK RADIOSITY METHOD

It is very likely that the $(\mathbf{RF})$ matrix included in Equation 2 has a low numeric rank. This is because each row $(\mathbf{RF})_i$ is computed based on the scene view from the element i, and most pairs of close patches have a very similar view of the scene (Figure 1). Then $(\mathbf{RF})$ has many similar rows, which results in a reduction of the numerical rank.

The rank reduction of $(\mathbf{RF})$ matrices allows approximating them by the product of two matrices $\mathbf{U}_k\mathbf{V}_k^T$, both with dimension $n \times k$ ($n \gg k$), without losing relevant information about the scene.

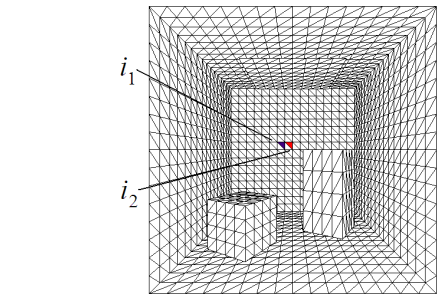

(a) Two close patches i_1 and i_2.

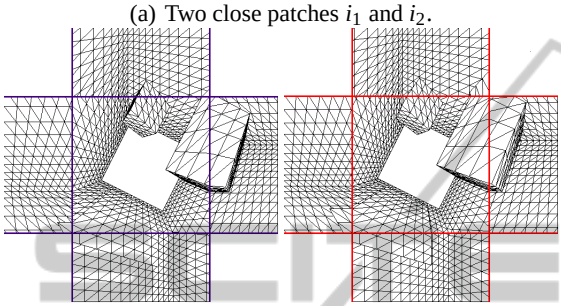

(b) Hemicube view from i_1. (c) Hemicube view from i_2.

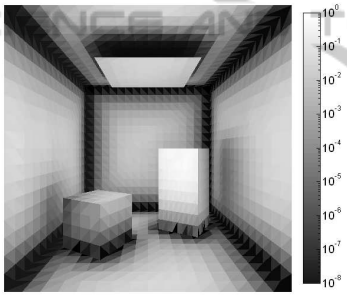

(d) Spatial coherence in the scene.

Figure 1: Close patches have similar views of the scene and generate similar rows in (**RF**). In (d) the spatial coherence of each patch is measured (darker means lower coherence).

3.1 Low-rank Approximation

The product $\mathbf{U}_k\mathbf{V}_k^T$ generates a matrix with dimension $n \times n$ and rank k. The memory space needed to store $\mathbf{U}_k$ and $\mathbf{V}_k^T$ is $O(nk)$, significantly less than the $O(n^2)$ required to store the matrix (**RF**), especially when $n \gg k$. This memory saving allows reducing the space needed to store the information for large scenes.

In the *LRR equation* (3), (**RF**) is replaced by the low-rank approximation $\mathbf{U}_k\mathbf{V}_k^T$. The unknown is not longer B, but an approximation $\widetilde{B}$ of the radiosity.

$$\left(\mathbf{I} - \mathbf{U}_k\mathbf{V}_k^T\right)\widetilde{B} = E \tag{3}$$

The matrix $\left(\mathbf{I} - \mathbf{U}_k\mathbf{V}_k^T\right)$ is easily invertible using the Sherman-Morrison-Woodbury formula (Golub and Loan, 1996). Equation 4 shows the expression for $\widetilde{B}$.

$$\widetilde{B} = E + \mathbf{U}_k\left(\left(\mathbf{I}_k - \mathbf{V}_k^T\mathbf{U}_k\right)^{-1}\left(\mathbf{V}_k^T E\right)\right) \tag{4}$$

In order to find $\widetilde{B}$ through Equation 4, $O(nk^2)$ operations are required and $O(nk)$ memory is needed.

In scenes with static geometry and dynamic lighting (i.e., only the independent term E varies in Equations 2 to 4), part of the computation can be executed before the real-time stage. Equation 4 is transformed into 5, where the $n \times k$ matrices $\mathbf{Y}_k$, $\mathbf{U}_k$, and $\mathbf{V}_k$ are calculated once. Thus, the real-time stage only has complexity $O(nk)$. This is an auspicious result in order to develop a new methodology for real-time radiosity.

$$\widetilde{B} = E - \mathbf{Y}_k\left(\mathbf{V}_k^T E\right), \tag{5}$$
$$\mathbf{Y}_k = -\mathbf{U}_k\left(\mathbf{I}_k - \mathbf{V}_k^T\mathbf{U}_k\right)^{-1}$$

Equation 5 can also be formulated as $\widetilde{B} = \mathbf{G}E$, so $\mathbf{G} = \mathbf{I} - \mathbf{Y}_k\mathbf{V}_k^T$ is considered as the global operator that manages the infinite bounces of light in a single operation. This global operator is computed without the use of Neumann series, as in (Kontkanen et al., 2006; Lehtinen et al., 2008), taking advantage of the fact that (**RF**) is a low-rank matrix.

3.2 $\mathbf{U}_k$ and $\mathbf{V}_k$ Calculation

$\mathbf{U}_k$ and $\mathbf{V}_k$ can be computed using factorization techniques, such as singular value decomposition (SVD or PCA) (Golub and Loan, 1996), CUR factorization (Goreinov et al., 1997), and discrete transformations based on Fourier and wavelets (Press et al., 2007). SVD is the only method that produces good approximations to (**RF**) for low values of k, but it has an $O(n^3)$ complexity. The other methods mentioned have lower complexity orders, but they also produce larger errors in the (**RF**) approximation.

To overcome the weakness of the traditional factorization techniques, the Low-Rank Radiosity (LRR) method proposed in (Fernández, 2009) uses the concept of *spatial coherence* (Sutherland et al., 1974). This method generalizes the two-level hierarchy methodology (Cohen et al., 1986), where two meshes with different granularity levels are generated for the scene (a *coarse mesh* with k patches and a *fine mesh* with n elements). Using these two meshes it is possible to build the $n \times k$ matrices $\mathbf{U}_k$ and $\mathbf{V}_k$.

Both, the coarse and the fine meshes, can be uniform or nonuniform. In this paper, we proposed a nonuniform coarse mesh that is adapted to the spatial coherence of the scene. In the resulting algorithm, named *2 Meshes with Spatial Coherence* (2MSC), the fine mesh is given, assuming that inside each element there is spatial coherence, but the coarse mesh is built taking care of the spatial coherence inside each patch.

The 2MSC produces a nonuniform mesh, with smaller patches in those areas with low spatial coherence. Algorithm 1 shows a *top-down* procedure for

creating the coarse mesh from a few large patches, using the 2MSC algorithm. An initial set of large patches are inserted into a list L (see Figure 2 (a)). Every patch is taken from L, one at a time. All patches without spatial coherence (i.e., when the inner scene views vary more than a specified threshold) are split into several subpatches, which are inserted into L. The algorithm stops when the list L is empty (i.e., when all patches have spatial coherence), or when all those patches without spatial coherence are smaller than a predefined value (A_{min}). The number of patches (k) depends on the value of the parameter A_{min} and also depends on the procedure used to evaluate the spatial coherence. Figure 2 (b, c) shows a coarse mesh generated using the 2MSC algorithm and a fine mesh. The discretization of the coarse mesh shown in Figure 2 (b) agree with the colors of spatial coherence shown in Figure 1 (d), i.e., the darker the color, the more need to split the surface.

Algorithm 1: 2MSC algorithm.

```
1: Store patches p in a list L.
2: while (L≠{}) do
3:     Remove a patch p from L.
5:     if ¬(spatial coherence inside p) ∧ (Area(p) > A_min)
6:         Divide p in subpatches and store them in L.
7:     end.
8: end.
```

After the scene meshes are defined, the matrices $\mathbf{U}_k$ and $\mathbf{V}_k$ are built using the information from an assignment function $P : e \rightarrow p$ that gives, for each element e in the fine mesh, the corresponding patch p in the coarse mesh. The assignment can be defined by inclusion (element e belongs to single patch p) or by proximity (p is the closest patch to element e).

If P is defined by inclusion and all elements belonging to any patch have equal area, the construction of matrices $\mathbf{U}_k$ and $\mathbf{V}_k$ follows Equation 6. There, $\mathbf{F}_{ep}$ is the form factor between an element e of the scene and the elements assigned to the patch p, and c_p is the number of elements assigned to p.

$$\mathbf{U}_k(e,p) = \mathbf{F}_{ep}/c_p$$
$$\mathbf{V}_k(e,P(e)) = 1\ ,\ \mathbf{V}_k(e,p) = 0\ \forall p \neq P(e) \qquad (6)$$

Other methodologies can be applied to build the matrices $\mathbf{U}_k$ and $\mathbf{V}_k$. Besides using SVD factorization, where the columns of both matrices are orthogonal, the columns of the matrix $\mathbf{U}_k$ generated using Equation 6 can also be orthogonalized using QR factorization. After the QR factorization is performed, a new matrix $\mathbf{U}_{QR}$ is generated and $\mathbf{V}_k$ can be replaced by $\mathbf{V}_{QR} = (\mathbf{RF})^T\mathbf{U}_{QR}$. These methodologies have been implemented by the authors to generate $\mathbf{U}_k$ and $\mathbf{V}_k$, and the experiments showed no conclusive results about which is best method. In this paper, the Equations in 6 were employed to build the matrices, due to both the simplicity of building a low rank approximation of the $(\mathbf{RF})$ matrices and the possibility to build a sparse version of the $\mathbf{V}_k$ matrix, as it is explained in the next section.

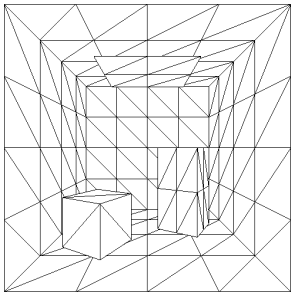

(a) Original coarse mesh.

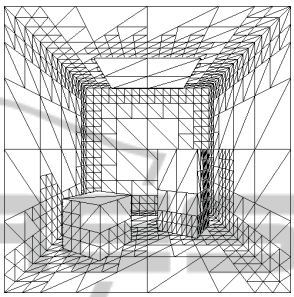

(b) Coarse mesh after 2MSC.

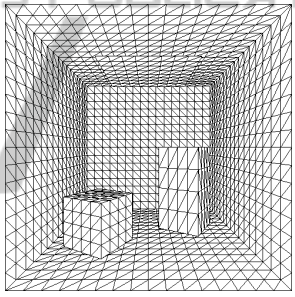

(c) Fine mesh.

Figure 2: Meshes used to compute $\mathbf{U}_k$ and $\mathbf{V}_k$.

4 SPARSE MATRICES IN LRR

The 2MSC algorithm and the Equations 6 generate sparse matrices $\mathbf{V}_k$ with dimension $n \times k$, with a unique non-zero entry in each row (corresponding with the $P(e)$ column). This section introduces an $O(k)$ storage methodology for the $\mathbf{V}_k$ matrix, and an implementation of the LRR method for both CPU and GPU platforms.

4.1 Compressing the Information in $\mathbf{V}_k$

The rows of $\mathbf{V}_k$ can be reordered, grouping them by the column where the non-zero value is in (k disjoint groups are created, see Figure 3). Using ideas from the compressed storage of sparse matrices (Barrett et al., 1994), an index vector I can be defined. I indicates that the rows of $\mathbf{V}_k$ with a one in the first column are placed from $I_1 = 1$ to $I_2 - 1$, that the rows of $\mathbf{V}_k$ with a one in the second column are placed from I_2 to $I_3 - 1$, and so on. The $O(k)$ entries of I are enough to define the matrix $\mathbf{V}_k$.

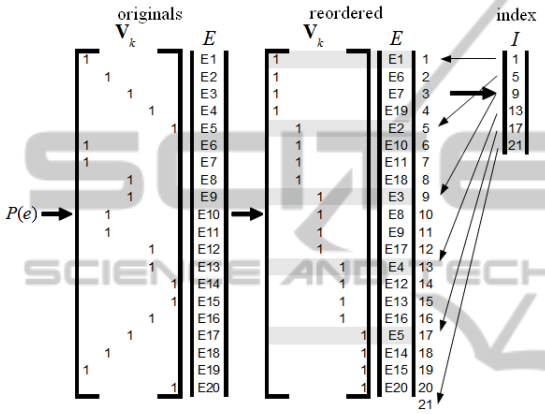

Figure 3: Construction of $\mathbf{V}_k$ and I from the function P.

Once the vector I is built and the values in the vector E are reordered accordingly to the rows of $\mathbf{V}_k$, the product $\mathbf{V}_k^T E$ can be formulated as the sum in Equation 7. The i-th value of the vector $\mathbf{V}_k^T E$ is the sum of the values of E between the positions I_i and $I_{i+1} - 1$.

$$\left(\mathbf{V}_k^T E\right)_i = \sum_{s=I_i}^{I_{i+1}-1} E_s \, , \forall i, 1 \leq i \leq k \qquad (7)$$

The previously presented results allow to conclude that if $\mathbf{V}_k$ is a sparse matrix with the stated properties, the matrix-vector product $\mathbf{V}_k^T E$ can be computed in $O(n)$ operations (instead of the $O(nk)$ operations needed when $\mathbf{V}_k$ is a full matrix).

4.2 Sparse LRR Implementation

In order to validate the theoretical results presented in the previous subsection, two implementations of the sparse LRR method were developed to solve the radiosity problem with a sparse $\mathbf{V}_k$ matrix generated by Equations 6. Each implementation uses a different hardware to perform the calculations: one uses a traditional CPU, and the other uses a GPU.

The LRR implementation in CPU uses the BLAS library (Lawson et al., 1979), and Equation 7 is solved sequentially. On the other side, the LRR implementation in GPU uses the CUBLAS implementation of BLAS for CUDA (NVIDIA, 2008), and k threads are used to update the vector $\left(\mathbf{V}_k^T E\right)_i$ in parallel, each thread computing $\sum_{s=I_i}^{I_{i+1}-1} E_s$ for a different i.

Both LRR implementations use the `xGEMV` function from the BLAS library to compute the matrix-vector product $\mathbf{Y}_k^T(\mathbf{V}_k^T E)$. The product $\mathbf{V}_k^T E$ is not explicitly computed, instead, it is calculated using the sum in Equation 7. The pseudocode of both implementations for a real-time processing of frames from a graphic application is sketched in Algorithm 2.

Algorithm 2: Sparse LRR.

{**Pre-processing:** Compute $\mathbf{Y}_k$ and I}
1: [ONLY CPU] Store $\mathbf{Y}_k$, I into RAM memory
2: [ONLY GPU] Send and store $\mathbf{Y}_k$, I into GPU memory
3: for each frame **do** {in real-time}
4: Receive E from a graphic application
5: **[ONLY GPU]** Send and store E into GPU memory
6: Compute $X_i = \left(\mathbf{V}_k^T E\right)_i, \forall i, 1 \leq i \leq k$, with $\sum_{s=I_i}^{I_{i+1}-1} E(s)$
7: Apply xGEMV to compute $\widetilde{B} = E - \mathbf{Y}_k^T X$
8: **[ONLY GPU]** Send $\widetilde{B}$ to RAM memory
9: Store $\widetilde{B}$ into RAM memory
10: end

5 EXPERIMENTAL ANALYSIS

The experimental analysis compares the time required to compute $\widetilde{B}$ using the LRR method, based on full and sparse matrices, as well as on CPU and GPU architectures.

5.1 Execution Platforms

A first analysis was performed in a Pentium dual-core E5200 (2.50 GHz), 2 GB RAM, with a NVIDIA 9800 GTX+ 512 MB. A second analysis using only sparse matrices and larger scenes was executed in a Tesla Intel Xeon QuadCore E5530 (2.27 GHz), 8 GB RAM, with a NVIDIA c1060 (240 cores at 1.3 GHz) 4 GB.

5.2 Test Scenes

A first analysis was performed using a *Cornell box* with several discretizations (n= {3456, 13824, 55296, 221184} and k= {216, 864, 3456}). For the experiments in the Tesla platform, six scenes with dimension ($n \times k$) 1769472×216, 221184×3456, 442368×1728, 884736×864, 1769472×432, and 3538944×216 were created from the same Cornell

box scene. Finally, we perform tests on a two-floor patio model with dynamic lighting changes.

5.3 Experimental Results

In the following tables, the row categorization puts together all scenes with approximately equal memory consumption. Each category consumes four times more memory than the previous one.

Table 1 shows the speedup values (ratio of execution times) obtained when computing $\mathbf{V}_k^T E$ using the sparse LRR implementations in GPU and CPU, and the comparison with the full matrix implementation. The best speedup values are shown in bold font.

The experimental results show that the speedup values were up to **335.50** in CPU, and up to **37.47** in GPU. The best speedup values were obtained for the scene with dimension 13824×3456, taking advantage of the large number of calculations in the sum and the parallel computing strategy in `xGEMV`. Table 1 also indicates that the sparse $\mathbf{V}_k^T E$ product is faster in CPU.

Table 1: Speedup when computing $\mathbf{V}_k^T E$.

dimension	$\frac{\text{fullCPU}}{\text{sparseCPU}}$	$\frac{\text{fullGPU}}{\text{sparseGPU}}$	$\frac{\text{sparseCPU}}{\text{sparseGPU}}$	$\frac{\text{fullCPU}}{\text{sparseGPU}}$
3456 × 216	15.67	8.00	0.60	9.40
3456 × 864	68.33	9.00	0.60	41.00
13824 × 216	21.67	11.36	0.64	13.93
3456 × 3456	75.75	18.33	**0.67**	50.50
13824 × 864	92.11	13.21	0.64	59.21
55296 × 216	17.42	11.20	0.64	11.20
13824 × 3456	**335.50**	**37.47**	**0.67**	**223.67**
55296 × 864	94.03	13.09	0.65	61.55
221184 × 216	24.01	10.99	0.58	13.84

Table 2 shows the speedup values when computing $\widetilde{B}$. These results demonstrate that the sparse implementation is about two times faster than the full implementation in CPU. Regarding the GPU implementations, the speedup values were between **5.21** and 2.05, and the best results were obtained when $k = 216$. Since 216 is not a multiple of 32, the GPU computing capacities are not fully used (Barrachina et al., 2008), and better speedup values shall be expected for other values of k. The computation of $\widetilde{B}$ is faster in GPU, despite that $\mathbf{V}_k^T E$ is faster in CPU.

Table 3 summarizes the speed of the LRR implementations regarding the number of frames per second (fps) that they are able to compute.

The results in Table 3 show that the minimum fps rate in CPU for the sparse LRR implementation (23 fps) is twice the value of the full LRR implementation from the previous work. In GPU, the minimum speed largely increased from 23 fps to 116 fps with the sparse LRR implementation. For the small scene

Table 2: Speedup when computing $\widetilde{B}$.

dimension	$\frac{\text{fullCPU}}{\text{sparseCPU}}$	$\frac{\text{fullGPU}}{\text{sparseGPU}}$	$\frac{\text{sparseCPU}}{\text{sparseGPU}}$	$\frac{\text{fullCPU}}{\text{sparseGPU}}$
3456 × 216	1.95	4.50	4.40	8.60
3456 × 864	1.69	2.38	6.48	10.93
13824 × 216	1.91	**5.21**	5.50	10.53
3456 × 3456	1.43	2.05	5.70	8.17
13824 × 864	1.88	3.41	9.73	18.32
55296 × 216	1.90	5.04	5.58	10.61
13824 × 3456	1.74	3.59	**11.34**	19.67
55296 × 864	1.95	3.62	10.95	**21.34**
221184 × 216	**2.05**	5.04	5.08	10.43

Table 3: Speed (fps) of the LRR implementations.

dimension	CPU		GPU	
	full	sparse	full	sparse
3456 × 216	**814**	**1591**	**1556**	**7000**
3456 × 864	221	372	1014	2414
13824 × 216	196	374	395	2059
3456 × 3456	70	100	278	569
13824 × 864	51	96	273	933
55296 × 216	47	90	100	504
13824 × 3456	14	24	76	275
55296 × 864	12	23	70	252
221184 × 216	11	23	23	116
Average	159	299	421	1569

with dimension 3456×216, a large fps rate of **7000** was achieved in GPU. Overall, the average speed values duplicate in CPU and quadruplicate in GPU, when compared the speed of the full LRR implementation.

5.4 Real-time LRR for Larger Scenes

The computational platform with the NVIDIA 9800 GTX+ GPU does not allow to scale up for computing the radiosity of scenes with a million polygons, due to its memory limitations. In order to show how the hardware evolution helps to solve the radiosity problem, six new larger scenes up to more than 3.5 million elements were solved in a Tesla GPU platform.

Table 4 presents the speed results (in fps) when using the Tesla platform to compute the radiosity for the three largest instances computed with the NVIDIA 9800 GTX+ GPU, and the speedup comparison with the Table 3. This analysis compares the capability of computing the radiosity in real-time using the new hardware. The fps rates in Table 4 shows that a significant speed improvement is obtained with the Tesla platform: it allows performing the radiosity computation in real-time, while speedup values up to **3.20** in CPU and **1.64** in GPU were achieved.

Table 5 summarizes the speed of the radiosity calculation for six new larger scenes up to 3.5 million elements in the Tesla platform. The scene with di-

Table 4: Comparative speed (fps) in the Tesla platform.

dimension	speed (fps)		speedup	
	CPU	GPU	CPU	GPU
13824 × 3456	**74.07**	297.87	3.06	1.09
55296 × 864	73.61	**301.72**	**3.20**	1.20
221184 × 216	72.92	190.74	3.18	**1.64**

mension 1769472×216 requires 8 times more memory than the largest scenarios in the previous subsection. Each of the other five scenes requires 16 times more memory than the largest scenarios in the previous subsection.

Table 5: Speed (fps) for larger scenes in the Tesla platform.

dimension	speed in CPU	speed in GPU
1769472 × 216	**8.15**	**24.05**
221184 × 3456	4.94	21.81
442368 × 1728	4.94	20.59
884736 × 864	4.55	18.67
1769472 × 432	4.10	15.45
3538944 × 216	4.00	11.48

The results in Table 5 demonstrate that the radiosity computation using the sparse LRR method can be performed in real-time in GPU, while none of the studied scenes can be computed in real-time in CPU. The GPU implementation was able to achieve a reasonable level of speed (around 20 fps) for scenes up to 1.7 million elements. A significant speed reduction was detected when solving the scene with more than 3.5 million elements, suggesting that there is still room to improve the proposed method in order to face even more complex scenarios.

Figure 4 show a wireframe view and three frames of an animated sequence for a patio building model, where the emission lights change for each frame. The complete video can be seen at www.fing.edu.uy/inco/grupos/cecal/cg/LRRSM.wmv. In the patio building (Figure 4), the dimension $(n \times k)$ is equal to 24128×1364 and the frame rate achieved is of 430 fps.

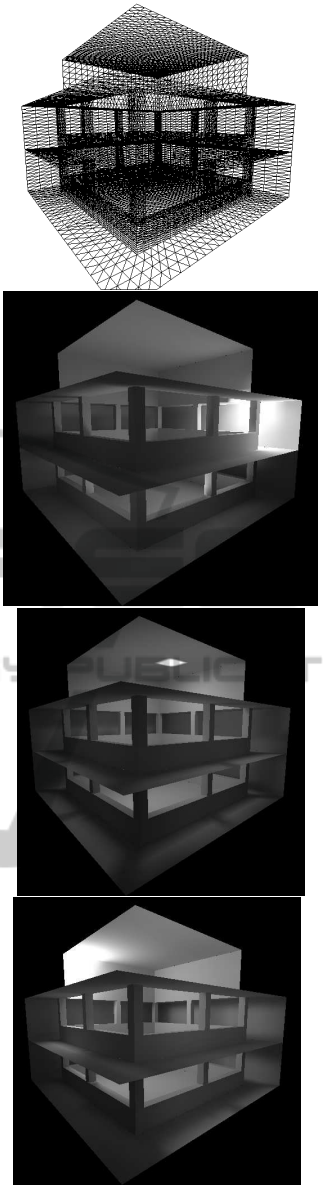

Figure 4: Patio building model. A wireframe view, and three different frames of an animated sequence.

6 CONCLUSIONS AND FUTURE WORK

This work introduces the utilization of sparse matrices in the low-rank radiosity technique. Four implementations of the LRR method (full/sparse matrices on CPU/GPU architectures) have been developed to solve the radiosity problem, and several examples of sparse LRR calculation have been implemented on a powerful GPU platform for greater $n \times k$ scenarios.

The main contribution of this work consists in the inclusion of a sparse matrix implementation into the LRR method. By reordering and grouping the information, $\mathbf{V}_k$ is transformed into an index vector I which requires only $O(k)$ memory to store the same information. As a result, the averaged acceleration factor rises to four in GPU architectures, due to the implementation of $\mathbf{V}_k^T E$ product with $O(n)$ sums.

The proposed method was able to solve the radiosity calculation in real-time for scenes with more than 1.7 million elements in a Tesla GPU platform.

This result shows the degree in which the sparse LRR method has a better performance than the full LRR method.

Two main lines of future work can be directly inferred from this paper: to further improve the efficiency of the proposed method, and to develop new ways to build $\mathbf{U}_k\mathbf{V}_k^T$ factorizations. Regarding the first line of work, the speed of the radiosity calculation shall be reduced when using a hybrid strategy of simultaneous computation in CPU and GPU, taking advantage of the fast computation of the product $\mathbf{V}_k^T E$ in CPU. Respecting the second line of work, further research must be performed to know the relation between low-rank approximations of $(\mathbf{RF})$ and the relative error of $\widetilde{B}$. Preliminary results have shown that in many situations, SVD it is not the optimal factorization for the radiosity problem, because other factorizations (such as those presented in this paper) generate radiosity results with lower relative error.

Finally, another area of future work consists into face the problem of processing scenes with dynamic geometry in order to extend the applicability of this new technique.

ACKNOWLEDGEMENTS

This work was partially funded by Programa de Desarrollo de las Ciencias Básicas, Uruguay, and by the TIN2010-20590-C02-02 project from Ministerio de Educación y Ciencia, Spain.

REFERENCES

Barrachina, S., Castillo, M., Igual, F., Mayo, R., and Quintana-Orti, E. (2008). Evaluation and tuning of level 3 CUBLAS for graphics processors. In *Workshop on Parallel and Distributed Scientific and Engineering Computing*, pages 1–8, Miami, EE.UU.

Barrett, R., Berry, M., Chan, T. F., Demmel, J., Donato, J., Dongarra, J., Eijkhout, V., Pozo, R., Romine, C., and der Vorst, H. V. (1994). *Templates for the Solution of Linear Systems: Building Blocks for Iterative Methods, 2nd Edition*. SIAM, Philadelphia, PA.

Cohen, M., Greenberg, D., Immel, D., and Brock, P. (1986). An efficient radiosity approach for realistic image synthesis. *IEEE Comput. Graph. Appl.*, 6:26–35.

Cohen, M., Wallace, J., and Hanrahan, P. (1993). *Radiosity and realistic image synthesis*. Academic Press Professional, Inc., San Diego, CA, USA.

Cohen, M. F., Chen, S. E., Wallace, J. R., and Greenberg, D. P. (1988). A progressive refinement approach to fast radiosity image generation. *SIGGRAPH Comput. Graph.*, 22:75–84.

Dutre, P., Bala, K., Bekaert, P., and Shirley, P. (2006). *Advanced Global Illumination*. A. K. Peters, Ltd.

Fasshauer, G. E. (2006). Meshfree methods. In *Handbook of Theoretical and Computational Nanotechnology. American Scientific Publishers*, pages 33–97.

Fernández, E. (2009). Low-rank radiosity. In *Proceedings IV Iberoamerican Symposium in Computer Graphics*, pages 55–62, Isla Margarita, Venezuela.

Golub, G. and Loan, C. V. (1996). *Matrix Computations*. The Johns Hopkins University Press.

Goreinov, S., Tyrtyshnikov, E., and Zamarashkin, N. (1997). A theory of pseudoskeleton approximations. *Linear Algebra and its Applications*, 261:1–21.

Gortler, S. J., Schröder, P., Cohen, M. F., and Hanrahan, P. (1993). Wavelet radiosity. In *Proceedings of the 20th annual conference on Computer graphics and interactive techniques*, SIGGRAPH '93, pages 221–230, New York, NY, USA. ACM.

Hanrahan, P., Salzman, D., and Aupperle, L. (1991). A rapid hierarchical radiosity algorithm. *SIGGRAPH Comput. Graph.*, 25:197–206.

Keller, A. (1997). Instant radiosity. In *Proceedings of the 24th annual conference on computer graphics and interactive techniques*, pages 49–56, New York, NY, USA. ACM Press/Addison-Wesley Publishing Co.

Kontkanen, J., Turquin, E., Holzschuch, N., and Sillion, F. (2006). Wavelet radiance transport for interactive indirect lighting. In Heidrich, W. and Akenine-Möller, T., editors, *Rendering Techniques 2006 (Eurographics Symposium on Rendering)*. Eurographics.

Laine, S., Saransaari, H., Kontkanen, J., Lehtinen, J., and Aila, T. (2007). Incremental instant radiosity for real-time indirect illumination. In *Proceedings of Eurographics Symposium on Rendering 2007*, pages 277–286. Eurographics Association.

Lawson, C. L., Hanson, R. J., Kincaid, D. R., and Krogh, F. T. (1979). Basic Linear Algebra Subprograms for Fortran Usage. *ACM Transactions on Mathematical Software*, 5(3):308–323.

Lehtinen, J., Zwicker, M., Turquin, E., Kontkanen, J., Durand, F., Sillion, F. X., and Aila, T. (2008). A meshless hierarchical representation for light transport. *ACM Trans. Graph.*, 27:37:1–37:9.

NVIDIA (2008). *CUDA CUBLAS Library*. NVIDIA Corporation, Santa Clara, California.

Press, W., Teukolsky, S., Vetterling, W., and Flannery, B. (2007). *Numerical Recipes: The Art of Scientific Computing*. Cambridge University Press.

Sloan, P., Kautz, J., and Snyder, J. (2002). Precomputed radiance transfer for real-time rendering in dynamic, low-frequency lighting environments. *ACM Transactions on Graphics*, 21:527–536.

Sutherland, I., Sproull, R., and Schumacker, R. (1974). A characterization of ten hidden-surface algorithms. *ACM Computing Surveys*, 6:1–55.

Wang, R., Wang, R., Zhou, K., Pan, M., and Bao, H. (2009). An efficient GPU-based approach for interactive global illumination. In *SIGGRAPH International Conference and Exhibition on Computer Graphics and Interactive Techniques*, pages 1–8, New York, NY, USA. ACM.